Sensors and Materials, Vol. 13, No. 8 (2001) 445–460
MYU Tokyo

S & M 0461

Diagnostics of Semiconductor Devices beyond the Diffraction Limit of Light

Hiroaki Fukuda[1,2,*], Toshiharu Saiki[3,4] and Motoichi Ohtsu[1,5]

[1]Interdisciplinary Graduate School of Science and Engineering,
Tokyo Institute of Technology, 4259 Nagatsuda, Midori-ku, Yokohama 226–8502, Japan
[2]Research and Development Center, Richo Co., Ltd.,
16–1 Shineicho, Tsuzuki-ku, Yokohama 224–0035, Japan
[3]Kanagawa Academy of Science and Technology
3–2–1 Sakado, Takatsuku, Kawasaki 213–0012, Japan
[4]Depertment of Applied Physics, The University of Tokyo,
7–1 Hongo, Bunkyo-ku, Tokyo 113–8656, Japan
[5]Localized Photon Project, ERATO, Japan Science and Technology,
Tenko Building #17 687–1 Tsuruma, Machida-shi, Tokyo 194-0004, Japan

(Received April 20, 2001; accepted August 10, 2001)

Key words: near-field optical microscope, near-field photocurrent, *p-n* junction, minority carrier, diffusion length, Si device, GaAs device, fiber probe, dopant concentration

Near-field photocurrent measurements are applied to the diagnostics of the *p-n* junction of semiconductor devices beyond the diffraction limit of light. In order to probe the internal properties of these devices, modes of propagation into the sample are utilized, retaining high resolution as a result of the contribution of a penetration depth smaller than the aperture diameter of the probe. Near-field photocurrent measurements with multi-wavelength excitation are applied to investigate a lateral *p-n* junction grown on patterned GaAs(111)A. The slant angle of the *p-n* junction interface is determined to be 30±8°. The minority carrier diffusion lengths of the electron L_n and the hole L_p of the Si *p-n* junction are estimated to be 0.47±0.03 and 0.37±0.02 μm, respectively. Near-field photocurrent measurements are also applied to the *p-n* junction on a Si substrate under the reverse-bias condition in order to estimate the dopant concentration of the *p-n* junction. The full-width at half maximum (FWHM) of the cross-sectional profile of the near-field photocurrent signal varied upon changing the applied reverse-bias voltage, according to the resulting change in the thickness of the depletion region. From the measured reverse-bias dependence of the FWHM of the cross-sectional profile, the local dopant concentration of the Si substrate was estimated to be $3.5{\pm}0.4{\times}10^{16}$ cm^{-3}. This result shows good agreement with the dopant concentration ($3.1{\times}10^{16}$ cm^{-3}) evaluated from the device specifications for device fabrication.

*Corresponding author, e-mail address: fukuda@rdc.ricoh.co.jp

1. Introduction

The recent miniaturization of semiconductor devices and circuits has made their diagnostics and analyses more difficult. Nondestructive and direct characterization of the microstructure of semiconductor devices has emerged as an important approach to understanding and improving the performance of these devices. Existing analytical tools yield the measured device parameter averaged over a large area. The electron-beam induced current method (EBIC)[1,2] and optical-beam induced current method (OBIC)[3] have been employed as useful analytical tools which measure the diffusion length of the minority carriers. However in these methods, the spatial resolution is limited to ~1 μm, and sample contamination and damage are serious problems. In the OBIC method, the diffraction of light limits the resolution. The dopant concentration is an important issue in semiconductor devices because it directly affects the device characteristics. Secondary ion mass spectroscopy (SIMS), which has been widely used to measure the dopant profile of semiconductor devices, can damage the sample and also lacks spatial resolution capabilities.

The near-field optical microscope (NOM) has been employed for the spatially resolved observation of subwavelength structures on the surface by overcoming the diffraction limit of conventional optical microscopes. Furthermore, NOM has been applied for imaging nanometric biological specimens, spectroscopy of semiconductor devices, high-density optical storage, atom manipulation, and nanostructure fabrication.[4–5] The near-field photocurrent measurements carried out with a near-field optical microscope have revealed useful information on semiconductor *p-n* junctions.[6–8]

In this paper, we review our results of near-field photocurrent measurements of semiconductor devices. After presenting the principle of the near-field photocurrent measurement system in section 2, the fabrication technologies of probes will be described in section 3. In section 4, the interaction between the optical near-field and high-refractive-index materials will be presented. Section 5 presents the experimental results of the near-field photocurrent measurements on a lateral *p-n* junction grown on patterned GaAs(111)A and a Si *p-n* junction. Section 6 gives the summary.

2. Principle of the Near-Field Photocurrent Measurement System

Figure 1 shows the experimental setup and sample structure. Operation of the near-field optical microscope in the illumination mode (I mode), where the optical near-field is generated from the subwavelength aperture at the fiber tip, is currently the most common method of selectively illuminating the sample. The electrode configuration for near-field photocurrent measurements of the *p-n* junction is also depicted in this figure. In order to maintain near-field excitation, the shear-force technique[9,10] was employed to maintain the separation between the fiber probe and the sample surface of 20 nm. All measurements were carried out under ambient conditions.

For excitation, light from an Ar^+ laser (λ = 351, 458 and 515 nm), He-Ne laser (λ = 633 nm), and Ti:sapphire laser (λ = 780 and 830 nm) are coupled to the fiber probe. Using this light, the optical penetration depth of the semiconductor substrates can be tuned. When the

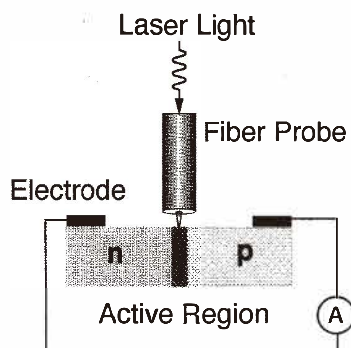

Fig. 1. Experimental setup of the near-field photocurrent measurements.

optical near-field of the fiber probe tip generates electron-hole pairs in the sample, the respective minority carriers diffuse away over an average diffusion length before the recombination. The induced near-field photocurrent signal is thus proportional to the number of carriers. The signal is collected at the electrodes while scanning the probe across the *p-n* junction. Then the collected signal is amplified with a current injection preamplifier and synchronously detected with a lock-in amplifier as a function of the position of the fiber probe across the surface of the *p-n* junction.

3. Fabrication of Probes

The fiber probe with the nanometer-scale aperture is the most essential device of the NOM. Several methods have been proposed for fabricating the probe.[4,5] A selective etching method using buffered hydrofluoric (HF) acid, which is widely employed in VLSI chip fabrication, is applied to sharpen an optical fiber. This method has achieved high reproducibility and realized a nanometer-scale tip diameter of the fiber probe. Section 3.1 describes the fabrication method of the high-sensitivity probe with a double-tapered structure. A novel fiber probe with a pure silica core is prepared for the ultraviolet (UV) near-field light source, which is described in section 3.2.

3.1 *Double-tapered fiber probe*

Figure 2(a) shows a scanning electron micrograph of the fiber probe used for the measurements. One of the advantages of a chemically etched probe is its extremely short light propagation length in a metal-cladding waveguide, which reduces the transmission efficiency of the probe.

An optical fiber with a germanium-dioxide (GeO_2)-doped core was used to fabricate the fiber probe. The core diameter of this fiber was 2 μm and the clad diameter was 125 μm. The fiber probe was fabricated by a two-step etching method.[4] The fiber was etched for 60 min in a buffered hydrogen fluoride (BHF) solution containing NH_4F (40 wt%), HF (50 wt%) and H_2O with the volume ratio of 1.7:1:1. Next, the fiber was etched for 40 min in

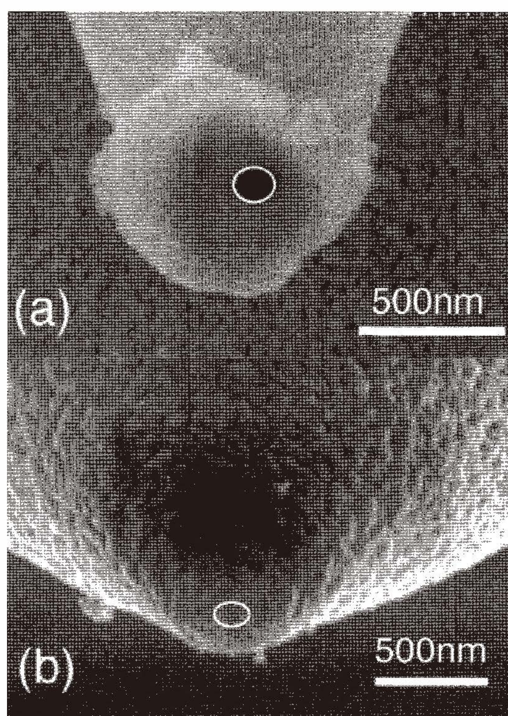

Fig. 2. Scanning electron microscope images of fiber probes. (a) Double-tapered fiber probe. (b) Fiber probe for UV region. White circle in these images represents the aperture. The diameters are 100 nm (a) and 150 nm (b).

NH_4F, HF and H_2O with the volume ratio of 10:1:1. The temperature of the BHF solution was maintained at 25 ± 0.1°C. The sharpened fiber probe was coated with 300-nm-thick Au. A subwavelength aperture was fabricated by pounding the metal-coated fiber probe on the Si substrate and squeezing the Au off to the side.[11] The diameter of the fabricated aperture was 150 nm.

The transmission efficiency was 5.0×10^{-3}, as estimated by collecting the far-field throughput with a 0.4-numerical-aperture objective lens.

3.2 *Fiber probe for UV region*

A novel fiber probe with a pure silica core is fabricated for the UV near-field light source. Because the conventional GeO_2-doped fiber exhibits strong optical absorption in the UV region, a single-mode fiber with a pure silica core and fluorine cladding is alternatively used to fabricate the fiber probe. The core diameter of this fiber is 10 μm and the clad diameter is 125 μm. After sharpening using a micropipette puller with a CO_2 laser as the heat source, the fiber probe is fabricated by selective chemical etching in BHF solution.[5,10]

Because of the pulling process, the diameter at the end of the tapered core is reduced to about 1 μm. The fiber is etched for 9 min in BHF containing NH_4F (40 wt%), HF (50 wt%) and H_2O with the volume ratio of 1.7:1:1. The temperature of BHF is 25 ± 0.1°C. This etching process is performed until the core is exposed from the cladding of fluoride-doped glass. To fabricate an aperture of subwavelength diameter (~100 nm), the sharpened fiber probe is coated with Al (300 nm thick).

The transmission efficiency is 1×10^{-5}, which is estimated by collecting the far-field throughput with a 0.4-numerical-aperture objective lens. Figure 2(b) shows a scanning electron micrograph of the fabricated fiber probe.

4. Interaction between Optical Near-Field and High-Refractive-Index Materials

The light emitted through the fiber probe has both optical near-field modes and propagating modes. The distribution of optical near-field modes in the tangential wave vector $k_{//}$ (component parallel to the surface) is determined by the aperture diameter d of the fiber probe. If d is less than half the wavelength $\lambda/2$ in free space, the optical near-field modes occupy the region $k_{//} > 2\pi/\lambda$. When the aperture of the probe is set close to an optically dense material, part of the optical near-field mode in the region $k_{//} < n(2\pi/\lambda)$ is converted to the propagating mode, where n is the refractive index of the material. Since Si is a much denser semiconductor material (refractive index of Si is ~5.44)[12] than the silica fiber probe (refractive index ~1.5) and surrounding air, almost all optical near-field modes from the fiber probe are coupled into propagating modes for the entire range of excitation wavelengths (λ = 351–515 nm). For the case of d = 150 nm and n = 4.58 (refractive index of Si at λ = 458 nm), almost all optical near-field modes from the fiber probe are coupled with propagating modes.

The propagating beam spread angle is determined by the aperture diameter. The cutoff wave vector of the optical near-field mode distribution lies at π/d.[7] The propagating beam spread angle is represented by $n(2\pi/\lambda)\sin\phi = \pi/d$. The dependence of the beam spread angle on the excitation wavelength is shown in Fig. 3 for d = 100, 150 and 200 nm. From these results, the beam spread angle of the light is found to be dependent on the excitation wavelength and the aperture diameter of the probe. The propagation modes are governed by the bulk absorption characteristics of the substrate material. Therefore, the resolution is limited by the aperture diameter, the penetration depth of the semiconductor material, and the diffusion length of photoexcited minority carriers.

5. Experimental Results

5.1 *Near-field photocurrent measurements of the lateral* p-n *junction of GaAs(111)A substrate*

Using the multiwavelength excitation light sources, near-field photocurrent measurements are applied to the lateral p-n junction on a patterned GaAs substrate.[13–15] A schematic of the sample structure is shown in Fig 4. After etching a semi-insulating

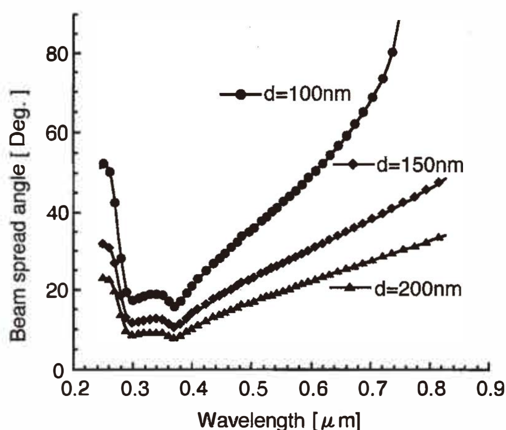

Fig. 3. Dependence of the beam spread angle of mode of propagation into Si on the excitation wavelength. d: aperture diameter.

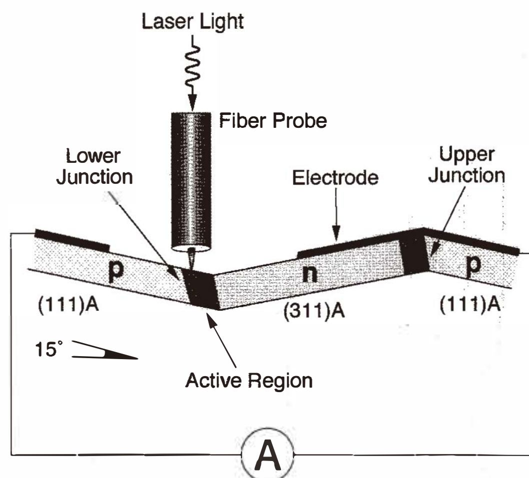

Fig. 4. Structure of lateral p-n junctions and experimental geometry. The lower junction was examined in this measurement. The sample was tilted by 15° in order to avoid contact with the cladding of the fiber probe.

GaAs(111)A substrate by the photolithography technique, 1-μm-thick Si-doped GaAs layers were grown by molecular beam epitaxy (MBE). The silicon concentration in the layer is 1×10^{-18} cm^{-3}. Due to the amphoteric nature of the Si dopant in GaAs, the lateral *p*-*n* junctions are formed at the upper and lower interfaces.(16,17)

A sharpened fiber probe was prepared by the two-step etching method described in section 3.1. After metallizing the exterior surface of the etched probe with 200-nm-thick

gold, a 200-nm-diameter aperture is fabricated by the resin coating method.[4] In order to realize high transmission efficiency, the shape of the tip is optimized by multistep chemical etching. The transmission efficiency is estimated as 1×10^{-3} with a 0.4-numerical-aperture objective lens. As multiwavelength light sources, the Ar^{+} laser (λ = 488 nm), He-Ne laser (λ = 633 nm), and Ti:sapphire laser (λ = 780, 830 nm) are coupled into the fiber probe. Using these light sources, the optical penetration depths in GaAs can be tuned from 80 nm to 1.0 μm.

Near-field photocurrent images at the excitation wavelengths of 488 and 830 nm are shown as topographic images in Fig. 5. Uniformity of the photocurrent intensity is seen along the *p-n* active region. The full-widths at half maximum (FWHMs) of the photocurrent signal profiles are 0.6 and 1.7 μm at λ = 488 and 830 nm, respectively. The increase of penetration depth results in the decrease of the resolving power. Figure 6 shows the cross-sectional profiles of photocurrent intensities in logarithmic scale. Due to the shallow penetration depth of 80 nm at the excitation wavelength of 488 nm, the resolution is

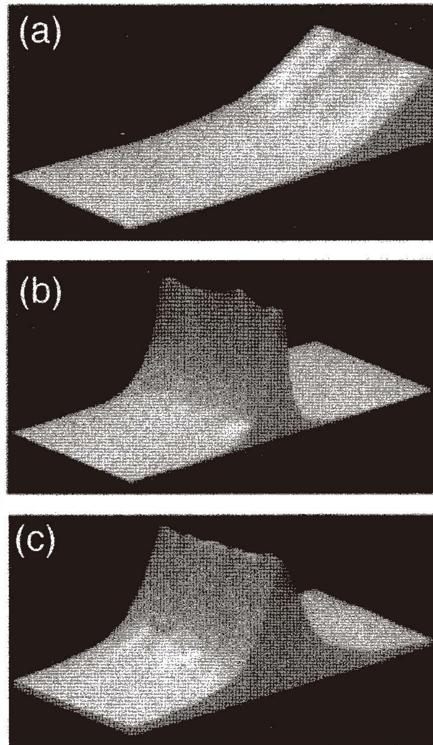

Fig. 5. Perspective views of the topographic image in the vicinity of lower junction (a), and the near-field photocurrent images at the excitation wavelength λ = 488 nm (b) and λ = 830 nm (c). The image size is 5×10 μm^2. The height of the slope in (a) is 1 μm.

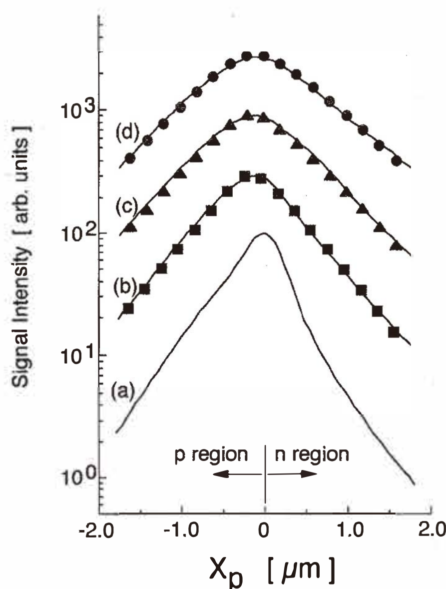

Fig. 6. Cross-sectional profiles of the near-field photocurrent signals at the excitation wavelengths λ = 488 nm (a), 633 nm (b), 780 nm (c), and 830 nm (d). Black circles, triangles, and squares represent the calculated results for ϕ = 40°, 37° and 27°, respectively, where θ = 15°.

governed by the aperture diameter and the diffusion lehgth of photogenerated minority carriers. Because of the difference in the diffusion length between electrons and holes, a large difference can be observed in the slower rise of the photocurrent signal in the *p* region than in the *n* region, which results in asymmetry of the signal profile. Moreover, with increasing penetration depth, the decay length increases and the asymmetric behavior reverses. The longer decay length in the *n* region than in the *p* region is due to the slant of the *p-n* interface.

The asymmetric signal behavior is analyzed using the one-dimensional model shown in Fig. 7. Here, the fitting parameters are the slant angle of the *p-n* junction interface θ and the beam spread angle ϕ. The application of this model to curves (b)–(d) in Fig. 6 is appropriate since, for the excitation wavelengths of 633, 780, and 830 nm, the respective penetration depths are much larger than those of the wavelengths in GaAs. With regard to the signal profile of λ = 488 nm, which is free from longer propagation into the sample, the characteristic decay length of the photocurrent signal due to the carrier diffusion effect is exactly imaged at least in the 200 nm region which is the aperture diameter of the fiber probe. Therefore, curve (a) in Fig. 6 depicts the spatial response profile of the *p-n* active region.

The spatial response profile of the *p-n* junction is described by the asymmetric form

$$F(x,z) = C \cdot \exp(x/L_n),\ x < -z \cdot \tan\theta$$
$$C \cdot \exp(x/L_p),\ x > -z \cdot \tan\theta, \qquad (1)$$

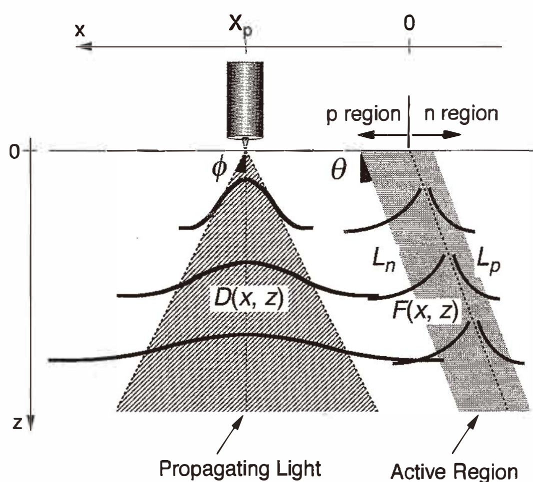

Fig. 7. Schematic of the slant *p-n* junction interface and the light propagating into the sample.

where C is a normalized constant, and L_p = 400 nm and L_n = 520 nm are the minority carrier diffusion lengths of the hole and the electron of GaAs, respectively.

For the angular distribution of light propagating into GaAs, we assume the Gaussian profile given by

$$D(x,z) = \frac{\exp\left[\dfrac{-(x-X_p)^2}{(z\cdot\tan\phi)^2}\right]}{z}, \tag{2}$$

where X_p indicates the position of the fiber probe and ϕ is a function of the excitation wavelength. The spatial distribution of light propagating into the substrate is expressed as

$$A(x,z) = \exp\left[\frac{-(x^2+z^2)^{1/2}}{L_{pd}}\right]. \tag{3}$$

The penetration depths L_{pd} for the excitation wavelengths of 633, 780, and 830 nm are 0.25, 0.65, and 1.0 μm, respectively. The intensity of the photocurrent signal is proportional to

$$I(X_p) = \int_0^d \int_{-\infty}^{\infty} D(x,z)A(x,z)F(x,z)dxdz, \tag{4}$$

where d =1.0 μm is the depth of the *p-n* junction interface.

The experimental curves (b)–(d) in Fig. 6 are perfectly fitted by eq. (4). From this calculation, we obtain the slant angle of the *p-n* junction interface, $\theta = 15 \pm 8^\circ$. The total slant angle of the *p-n* junction interface of $30 \pm 8^\circ$ to the *p* side, which is the sum of the observed slant angle θ of $15 \pm 8^\circ$ and intended tilt angle of 15° in the experimental setup, can be explained in terms of the nature of crystal orientation dependence of the growth.[18] The most significant reason is that the growth rate of GaAs on (311)A is faster than that on (111)A, which causes the shift of the *n*-type region to the *p* side on growth.

5.2 *Near-field photocurrent measurements of Si* p-n *junction*

Near-field photocurrent measurement using multiwavelength excitation sources is applied to evaluate the *p-n* junction of a Si bipolar transistor.[19] After removing the mold package of the bipolar transistor, the passivation layer and locally oxidized Si layer are etched by reactive ion etching. Furthermore, the surface of the *p-n* junction on the Si substrate is exposed by HF wet etching. The depth of the *p-n* junction interface is 0.6 μm. The slant angle of the Si *p-n* junction interface is $\theta = 0^\circ$ (shown as θ in Fig. 7). When using UV light for excitation, the small penetration depth decreases the region in which photoexcited carriers are generated. The minority carrier diffusion length is determined from near-field photocurrent signals. As a multiwavelength excitation light source, the output light beam from an Ar^+ laser (wavelength $\lambda = 351$, 458, and 515 nm) is coupled to the fiber probe. Using this light, the penetration depth in Si substrate can be tuned from 10 nm to 250 nm.[16] A novel fiber probe with a pure silica core, fabricated by the method described in section 3.2 (Fig. 2(a)), could be used as the UV near-field light source.

Figures 8(a), (b), and (c) show near-field photocurrent images for $\lambda = 351$, 458, and 515 nm, respectively. The cross-sectional profiles of the near-field photocurrent signals taken along the two arrows in these figures are shown in Fig. 9. The FWHMs of the cross-sectional profiles are 0.6, 0.9, and 1.1 μm, respectively. This wavelength dependence of the FWHM is due to that of the penetration depth. At the excitation wavelength of 351 nm, the resolution is determined by the aperture size of the fiber probe and the diffusion length of photogenerated carriers, because the penetration depth is shallow. Therefore longer excitation wavelength deteriorates the resolution.

By fitting eqs. (1) – (4) to the experimental values in Fig. 9, the diffusion lengths of minority carriers L_n and L_p are estimated to be 0.47 ± 0.03 and 0.37 ± 0.02 μm, respectively. This difference in the diffusion lengths between electrons and holes can be seen in this figure as the slower rise of the photocurrent signal in the *n* region than in the *p* region.

5.3 *Near-field photocurrent measurements of Si* p-n *junction under the reverse-bias condition*

In this section, we review our results of near-field photocurrent measurements for the reverse-bias *p-n* junction on a Si substrate and estimate the local dopant concentration of the *p-n* junction.[20] Figure 10 shows the experimental setup and sample structure. The sample preparation of the Si *p-n* junction has been described in section 5.2. A fiber sharpened by two-step etching with a 100 nm aperture fabricated by the method described in section 3.1 is used as a probe (Fig. 2(b)). The electrode configuration for near-field photocurrent measurements of the Si *p-n* junction under the reverse-bias condition is also

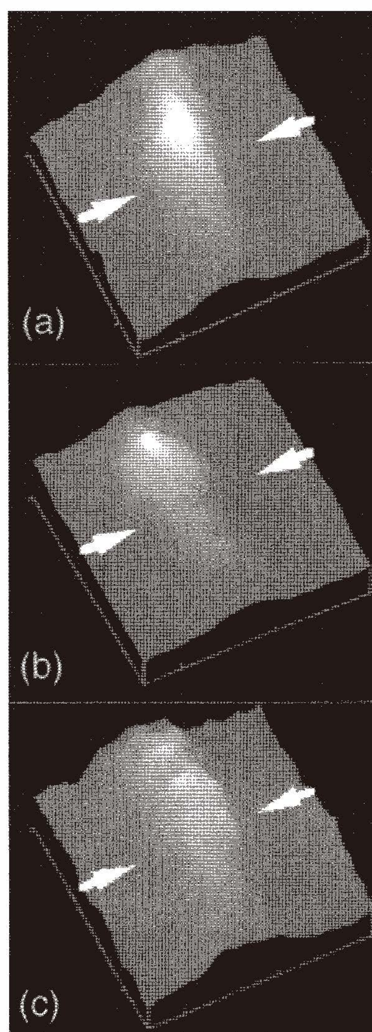

Fig. 8. Perspective views of the near-field photocurrent images at the excitation wavelengths λ = 351 nm (a), λ = 458 nm (b), and λ = 515 nm (c). The image size is 2.5×2.5 μm^2.

depicted in Fig. 10. The depth of the *p-n* junction in the substrate was 0.6 μm. The dopant concentration in the *n*-type region evaluated from the device fabrication condition is 3.1×10^{16} cm^{-3}.[21] For excitation, the light from an Ar^+ laser (λ = 458 nm) is coupled to the fiber probe. The penetration depth of this light into the Si substrate is estimated to be about 277 nm.

Figures 11(a), (b), and (c) show the near-field photocurrent images for the applied

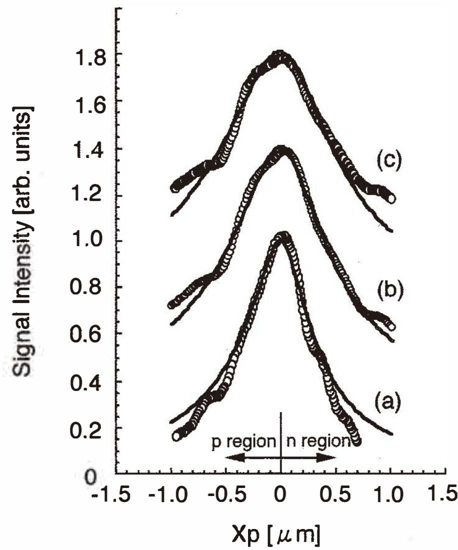

Fig. 9. Cross-sectional profiles of the near-field photocurrent signals at the excitation wavelengths λ = 351 nm (a), 458 nm (b), and 515 nm (c) taken along the two arrows in Figs. 8 (a), (b), and (c), respectively. The solid curves represent the results calculated from eq. (4).

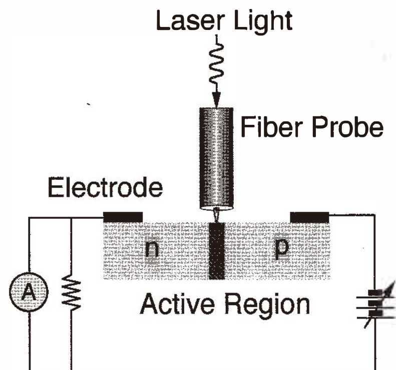

Fig. 10. Experimental setup and the cross-sectional structures of the sample.

reverse-bias voltages of 0 V, 3 V and 5 V, respectively. The uniformity of the decay length of the near-field photocurrent signals is clearly observed under the various reverse-bias conditions along the length of the p-n active region. Figure 12 shows the cross-sectional profiles of the near-field photocurrent intensities averaged over the measurement area. A clear peak of the cross-sectional profiles of the near-field photocurrent signals can be obtained by positioning the aperture above the depletion region. The FWHM of the cross-sectional profiles of the near-field photocurrent signal increases with increasing reverse-

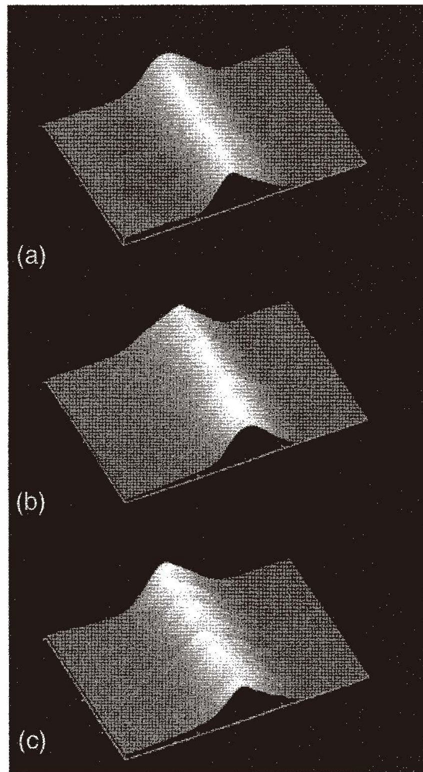

Fig. 11. Perspective views of the near-field photocurrent images under the reverse-biased voltages of 0 V (a), 3 V (b) and 5 V (c). The image size is 6×4 μm^2.

bias voltage.

The width of the cross-sectional profile of the near-field photocurrent signal increases according to the increase in the thickness of the depletion region with increasing reverse-bias voltage. Because the decay length of near-field photocurrent signals is constant regardless of the reverse-bias conditions, the relationship between the FWHM of the cross-sectional profile of the near-field photocurrent $W(V_R)$ and the thickness of the depletion region $D(V_R)$ under reverse-bias voltage V_R is described by

$$W(V_R) = D(V_R) + C\,, \tag{5}$$

where C is a constant. Because the depth of the junction is shallow, $D(V_R)$ is described by the one-side step junction approximation,[22] and is expressed as

$$D(V_R) = \sqrt{2\varepsilon \frac{(V_R + \phi_B)}{q \cdot N_D}}\,, \tag{6}$$

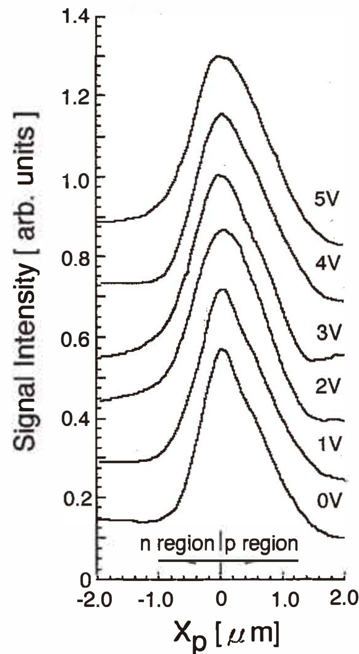

Fig. 12. Cross-sectional profiles of the near-field photocurrent signals under various reverse-biased voltages.

where N_D is the dopant density in the n-type sample, ε is the dielectric constant of Si, ϕ_B = 0.7 V is the built-in voltage, and q is the electron charge. From eqs. (5) and (6), the difference in the FWHM of the cross-sectional profile of the near-field photocurrent between the reverse-bias V_R condition and no-bias condition is represented by

$$W(V_R) - W(0) = \sqrt{\frac{2\varepsilon}{q \cdot N_D}} \cdot \left(\sqrt{V_R + \phi_B} - \sqrt{\phi_B}\right). \tag{7}$$

From this equation, we obtain the dopant density N_D in the Si substrate.

Figure 13 shows the dependence of the FWHM of the cross-sectional profile of the near-field photocurrent signals under the reverse-bias condition obtained from Fig. 12. The reverse-bias voltage is varied from 0 V to 5 V. Upon increasing the reverse-bias voltage, the FWHM of the cross-sectional profiles of the near-field photocurrent signal increases. By substituting the slope of the line fitted to the measured values into eq. (7), the value of N_D in the n-type region is estimated to be $3.5 \pm 0.4 \times 10^{16}$ cm^{-3}. This is consistent with the dopant concentration (3.1×10^{16} cm^{-3}) evaluated from the design specifications of

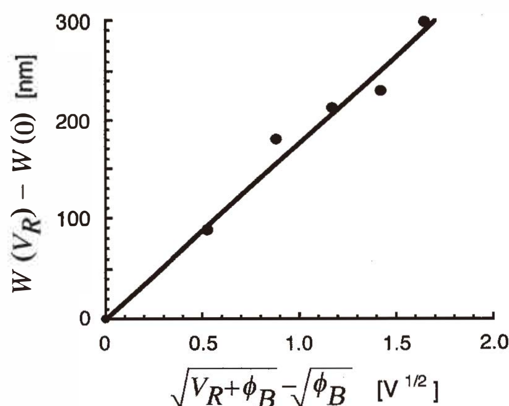

Fig. 13. Relationship between the reverse-biased voltage and the differential of the FWHM of the cross-sectional profile of the near-field photocurrent signals.

device fabrication. This result establishes a simple relationship between the FWHM of the cross-sectional profiles of the near-field photocurrent signal and the applied reverse-bias voltage. Thus, such measurement can be utilized as a simple nondestructive and local method for estimating the dopant concentration of semiconductor substrates and devices.

6. Summary

We have reviewed the application of near-field photocurrent measurements to the diagnostics of *p-n* junctions of semiconductor devices beyond the diffraction limit of light. Using multiwavelength excitation sources, we demonstrated that the near-field photocurrent measurement applied to the lateral *p-n* junctions of GaAs and Si is a powerful technique for investigating not only the surface properties but also the internal structure of bulk devices with high spatial resolution. When the aperture of the probe was close to an optically dense material, the optical near-field modes from the fiber probe were coupled to propagating ones. Since the propagation modes are governed by the bulk absorption characteristics of the substrate material, the resolution is limited by the size of the aperture diameter and the penetration depth of the semiconductor material.

The optical penetration depth into the semiconductor materials depends on the wavelength of the light sources. The increase of penetration depth results in the decrease of the resolution. The smallest penetration depth gives the spatial response profile of the active region, including the carrier transport properties, at the resolution of the aperture diameter.

Near-field photocurrent measurements with multiwavelength excitation were applied to investigate a lateral *p-n* junction grown on patterned GaAs(111)A. The slant angle of the *p-n* junction interface was determined to be $30 \pm 8°$. The minority carrier diffusion lengths for electrons L_n and holes L_p of the Si *p-n* junction were estimated to be 0.47 ± 0.03 and 0.37 ± 0.02 μm, respectively, from the near-field photocurrent signals. Near-field photocurrent

measurements were also applied to the *p-n* junction on a Si substrate under the reverse-bias condition in order to estimate the dopant concentration of the *p-n* junction. By increasing the reverse-bias voltage of the *p-n* junction, the FWHM of the cross-sectional profile of the near-field photocurrent signal increased according to the extent of the depletion region. From these results, the local dopant concentration N_D in the *n*-type region was estimated to be $3.5 \times 0.4 \times 10^{16}$ cm^{-3}. This result is consistent with the dopant concentration (3.1×10^{16} cm^{-3}) evaluated from the design specifications of device fabrication. From these results, tomographic diagnostics using the near-field photocurrent measurements method will provide new insight for understanding the characteristics of semiconductor devices and photonic devices, and enable reliability studies of industrial semiconductors and failure analysis of semiconductor devices.

References

1 H. J. Leamy: J. Appl. Phys. **53** (1982) R51.
2 W. H. Hackett, Jr.: J. Appl. Phys. **43** (1972) 1649.
3 H. Komoda and K. Shimizu: Jpn. J. Appl. Phys. **33** (1994) 3393.
4 M. Ohtsu: Near-Field Nano/Atom Optics & Technology (Springer-Verlag, Tokyo, 1998).
5 M. Ohtsu: J. Lightwave Technol. **13** (1995) 1200.
6 S. K. Buratto, J. W. P. Hsu, E. Betzig, J. K. Trautman, R. B. Bylsma, C. C. Bahr and M. J. Cardillo: Appl. Phys. Lett. **65** (1994) 2654.
7 M. S. Unlu, B. B. Goldberg, W. D. Hrzog, D. Sun and E. Towe: Appl. Phys. Lett. **67** (1995) 1862.
8 K. Karrai, G. Kolb, G. Abstreiter and A. Schmeller: Ultramicroscopy **61** (1995) 299.
9 E. Betzig, P. L. Finn and J. S. Weiner: Appl. Phys. Lett. **60** (1992) 2484.
10 R. Toledo-Crow, P. C. Yang, Y. Chen and M. Vaez-Iravani: Appl. Phys. Lett. **60** (1992) 2957.
11 T. Saiki and K. Matsuda: Appl. Phys. Lett. **64** (1999) 2773.
12 E. D. Palik: Handbook of Optical Constants of Solids (Academic Press, Orlando, 1985).
13 T. Saiki, N. Saito, J. Kusano and M. Ohtsu: Appl. Phys. Lett. **69** (1996) 644.
14 N. Saito, F. Sato, K. Takizawa, J. Kusano, H Okumura, T. Aida, T. Saiki and M. Ohtsu: Jpn. J. Appl. Phys. **36** (1997) L896.
15 T. Saiki, S. Mononobe, M. Ohtsu, N. Saito and J. Kusano: Appl. Phys. Lett. **67** (1995) 2191.
16 J. M. Ballingall and C. E. C. Wood: Appl. Phys. Lett. **41** (1982) 947.
17 W. I. Wang, E. E. Mendez, T. S. Kuan and L. Esaki: Appl. Phys. Lett. **47** (1985) 826.
18 T. Nishinaga, K. Mochizuki, H. Yoshinaga, C. Sasaoka and M. Washijima: J. Cryst. Growth 98 (1989) 98.
19 H. Fukuda, Y. Kadota and M. Ohtsu: Jpn. J. Appl. Phys. **38** (1999) L571.
20 H. Fukuda and M. Ohtsu: Jpn. J. Appl. Phys. **40** (2001) L286.
21 T. Hyodo, N. Yoshida and H. Watanabe: Ricoh Technical Report **23** (1997) 19.
22 A. S. Grove: Physics & Technology of Semiconductor Devices (John Wiley & Sons Inc., New York, 1967).